Proceedings of 2022 Responsible Engineering and Living Symposium
Windsor, Ontario, Canada
June 23-24, 2022

Bio-inspired study of thermal effects on NACA0012 airfoil at Reynolds Number of 33,000

Mohd Sahil Akhtar
Soft Materials Research Laboratory, Department of Chemical Engineering,
National Institute of Technology Karnataka, Surathkal, Mangalore 575025, Karnataka, India

David S-K. Ting
Turbulence and Energy Laboratory, University of Windsor
401 Sunset Ave, Windsor, ON, Canada

Jagannathan T. Kalathi
Soft Materials Research Laboratory, Department of Chemical Engineering,
National Institute of Technology Karnataka, Surathkal, Mangalore 575025, Karnataka, India

Abstract

The amount of solar and background radiation absorbed by birds vary according to their wing shape, pigmentation, porosity, etc. Birds are equipped with unique features to thrive, including attracting opposite sex, regulating body temperatures, and soaring in the sky. The research focuses on solar/sky radiation by examining how NACA0012 airfoil, representing the wing of a bird, performs when its upper surface temperature is higher or lower than the surrounding air. This is realised by performing 2-dimensional simulations in OpenFOAM at a Reynolds Number of 33,000, where Spalart-Allmaras model is used to simulate the flow turbulence. The upper surface of the airfoil is warmed to 330 K and cooled to 270 K at a pressure of 1 atm, an ambient temperature of 300 K, and a Mach number of 0.0725. The results illustrate the airfoil with the cooler top surface exhibits a lower drag and higher lift than its warmer top surface counterpart. A maximum reduction of drag coefficient from 0.065 to 0.061 and increase in lift coefficient from 0.89 to 0.93 at an angle of attack 11° are achieved. In short, tuning the upper surface of NACA0012 airfoil to temperatures lower than the ambient provides better aerodynamic performance.

Keywords: Background radiation, NACA0012 airfoil, Lift-Drag Coefficient, OpenFOAM, Spalart-Allmaras model.

Nomenclature

A	Area of airfoil	p	Pressure
AOA	Angle of attack	$\dot{q}_s$	Rate of heat transfer per unit area
c	Chord length of the airfoil	$\dot{q}_v$	Rate of heat source/sink per unit volume
C_D	Drag coefficient	R	Gas constant
C_L	Lift coefficient	RANS	Reynolds Averaged Navier-Stokes
CM	Airfoil control mass	Re	Reynolds number
CV	Airfoil control volume	S	Airfoil control surface
D	Drag force acting on the airfoil	$T, \Delta T$	Temperature, temperature difference
e	Total energy per unit mass	T_a, T_l, T_u	Ambient, lower, and upper temperature
f	Net force acting on a body	v	Free stream velocity
f_b	Body force	δ	Thickness of airfoil
f_s	Surface force	V	Volume of control volume
L	Lift force acting on the airfoil	μ	Viscosity
m	Mass of airfoil control mass	ρ	Density
Ma	Mach Number		

Introduction

There has been a lot of focus on drone design in the past years. Their essential qualities, including effortless deployment, adjustable altitude, flexibility, and mobility can be attributed to their rising popularity and continued research [Shakeri et al., 2019]. They are ideally suited for a wide range of practical applications, including but not limited to the military and civil sectors [Shakhatreh et al., 2018]. Their versatility signals the beginning of a new era in which unmanned aerial vehicles, in addition to surveillance and remote sensing, are gaining ground in many important industries for non-destructive testing and the early detection of catastrophic failures [Balestrieri et al., 2021]. In addition to improvements in existing designs, research has also furthered the development of unique drones of different shapes, sizes, and weights [Yu, 2018]. Therefore, the configuration of drones varies greatly depending on the platform and requirements of the operation. As a result, they are categorized in various ways based on several factors [Sultan et al., 2021]. The smaller aerial vehicles do, however, have one major weakness: their power system is insufficient to support extended flying durations [Townsend et al., 2020]. Finding an excellent alternative to increasing current unmanned aerial vehicles aerodynamic performance is thus necessary.

Several natural occurrences help to alter the way that innovation is perceived. It is critical to harness these occurrences considering the present energy crisis [Coyle & Simmons, 2014]. The want for energy has prompted more studies into improving performance to maximizing effectiveness by using nature as a doorway. Therefore, we can imitate birds to create techniques for lowering drag in all types of air and water transportation thanks to the science of biomimicry and bio-inspiration [Bushnell & Moore, 1991; Tucker, 1993]. Because birds are particularly effective flyers, bio-inspired drone design has promising advantages [Floreano & Wood, 2015].

The question of why the avian flight is so efficient does not come as a surprise. It is a sum of varying unique characteristics collectively optimized that helps them surpass the performance of any manufactured vehicle of an equivalent size [Hedenström, 2002]. One such attribute of birds that has gained interest over the years is coloration of birds. The wing coloration of birds such as albatrosses, shearwaters, sooty terns, and black swimmers influences their skin drag and plays a key role in its reduction [Hassanalian et al., 2017, 2018]. The upper and lower surfaces of the wing, being black and white respectively, affect the amount of solar/sky radiation absorbed due to the differing solar absorptivity, as shown in Fig. 1. Therefore, a temperature difference exists between the top and bottom wing surfaces. Measurements of the maximum average temperature show that the black wing can be heated to as much as 81.3°C while the white wing only heats to 53.1°C [Hassanalian et al., 2019]. Rogalla et al. [2019] showed that darker feathers warmed up to 70.7°C in the absence of wind, which was 31.0°C hotter than the brighter ones when exposed to solar radiation. Hassanalian et al. [2019] conducted experiments on different airfoil types using a temperature difference of 10°C between the wind tunnel and the top wing surface. Their investigations revealed a reduction in drag and lift improvement for almost all studied angle of attack (AOA) values. The aerodynamic performance, measured in dimensionless Lift and Drag coefficients (C_L and C_D), are described in terms of airfoil reference area (A) and chord length (c), under the influence of a Lift (L) and Drag (D) force, in a freestream of velocity (v), density (ρ) and viscosity (μ):

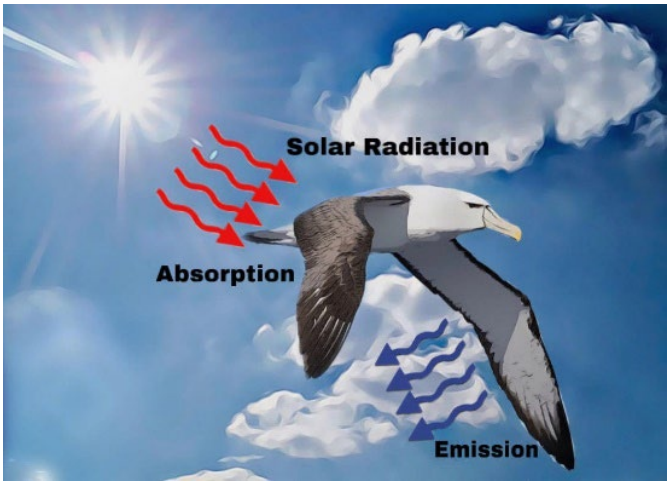

Fig. 1 Black and white wing coloration of an Albatross under solar radiation.

$$C_L = \frac{L}{1/2(A\rho v^2)} \quad (1)$$

$$C_D = \frac{D}{1/2(A\rho v^2)} \quad (2)$$

The values of C_D and C_L for different types of airfoils reported by Hassanalian et al. [2019] are provided in Table 1 at Re $\cong 10^5$, where Re is flow Reynolds number given by:

$$\mathrm{Re} = \frac{\rho v c}{\mu} \quad (3)$$

Their results suggest that aerodynamic performance was improved by upper surface heating. The C_D values decreased for all airfoils, with a maximum percentage drop in C_D (ΔC_D= 50%) noticed for the GOE174 airfoil. The maximum improvement in C_L (ΔC_L= 71%) was observed for the E186 airfoil. The best performance was exhibited by the same airfoil, for which C_L/C_D value increased by three folds.

Table 1 Summary of Lift improvement and Drag reduction by upper surface heating of 10°C on different airfoils [Hassanalian et al. 2019].

Airfoil	C_D *w/o heating*	C_D *with heating*	ΔC_D (%)	C_L *w/o heating*	C_L *with heating*	ΔC_L (%)	C_L/C_D *w/o heating*	C_L/C_D *with heating*	$\Delta(C_L/C_D)$ (%)
NACA2412	0.14	0.11	21 ↓	0.19	0.22	16 ↑	1.61	2.05	27 ↑
GOE174	0.06	0.03	50 ↓	0.18	0.25	39 ↑	2.50	7.10	184 ↑
S5020	0.07	0.06	14 ↓	0.12	0.14	17 ↑	1.32	1.80	36 ↑
E186	0.13	0.07	46 ↓	0.21	0.36	71 ↑	0.70	2.12	203 ↑
MH20	0.09	0.07	22 ↓	0.08	0.12	50 ↑	0.91	1.61	77 ↑

Table 2 Summary of effects of temperature* warmer and cooler than ambient on the performance of different airfoils.

Parameters	Norton et al. (1973)	Hinz et al. (2013)	Kim et al. (2003)	Bekka et al. (2009)	Samiee et al. (2018)
Airfoil	NACA0012-64	Pitching NACA0012	NACA0012	NACA0012	NACA2412
Re	750,000	3,000	33,000	38,000	3,000
Temperature	Wing-to-freestream temperature ratio increased from 1 to 2	$T_u = T_l$=350K T_a = 300 K	T_u = 200 K T_l = 400 K T_a = 300 K	T_u = 200 K T_l = 400 K T_a = 300 K	T_u = 200 K T_l = 400 K T_a = 300 K
C_L	Decrease from 1.00 to 0.70 ↓	Decrease from 0.86 to 0.75 ↓	Increase from 0.66 to 0.96 ↑	Increase from 0.85 to 1.17 ↑	Increase from 0.04 to 0.12 ↑
C_D	Increase from 0.006 to 0.009↑	Decrease from 0.37 to 0.35 ↓	Decrease from 0.120 to 0.062↓	Decrease from 0.130 to 0.082↓	Decrease from 0.073 to 0.071↓
Conclusion	Overall performance decreased	Overall performance decreased	C_L/C_D increase from 5.40 to 15.5	C_L/C_D increase from 6.64 to 14.27	C_L/C_D increase from 0.58 to 1.72

* the subscripts in T namely a, u, and l stand for ambient, upper, and lower surface temperature respectively.

Table 2 highlights studies contrary to the results of Hassanalian et al. [2019]. Norton et al. [1973] at Re $= 7.5 \times 10^5$ revealed that C_L decreased from 1.0 to 0.7 for NACA0012-64 airfoil wall temperature warmer than ambient. Hinz et al. [2013] studied NACA0012 at Re $= 3000$, ΔT = 50 K, T_a = 300 K and concluded decrease in C_L from 0.86 to 0.76 and C_D decrease from 0.37 to 0.35 . Kim et al. [2003] studied NACA0012 airfoil at Re $= 3.3 \times 10^4$ with $T_u = 200$ K and $T_l = 400$ K at $T_a = 300$ K and concluded increase in C_L/C_D from 5.4 to 15.5. Bekka et al. [2009] at Re $= 3.8 \times 10^4$ and thermal conditions same as Kim et al. concluded increase in C_L/C_D from 6.64 to 14.27. Samiee et al. [2018] studied NACA2412 at Re $= 3{,}000$ with $T_u = 200$ K, $T_l = 400$ K and $T_a = 300$ K and documented C_L/C_D increase from 0.58 to 1.72. In addition, Longo & Radespiel [1995] found that at Re $= 7.5 \times 10^5$, the C_L value decreases from 1.30 to 1.15 with NACA0012-64 airfoil upper surface temperature twice the ambient. The same methodology was implemented by Ribeiro et al. [2019] for applications in wind turbines. At Re $= 5.5 \times 10^5$, $T_u = 225$°C and $T_l = 25$°C the C_L/C_D ratio decreased from 33.2 to 20.4 for S809 airfoil whereas with $T_u = 25$°C and $T_l = 225$°C, almost no change was observed in the airfoil performance.

The above discussion highlights an existing contrast between the effects of warming and cooling of upper surface. While some studies show that cooling the upper surface of an airfoil increase performance [Bekka et al., 2009; Hinz et al., 2013; Kim et al., 2003; Samiee et al., 2018], Hassanalian et al. [2019] indicates otherwise.

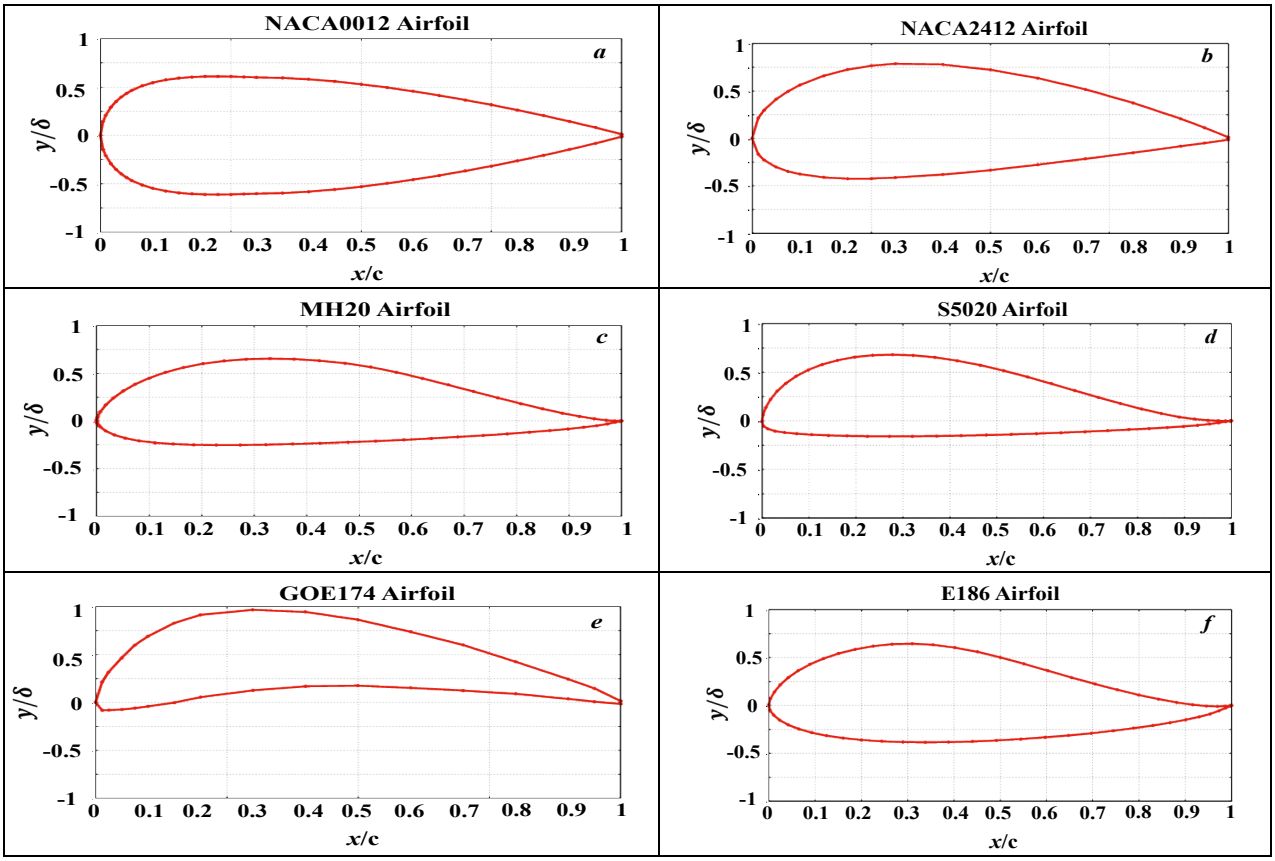

Fig. 2 Geometry of NACA0012 airfoil (c = 20 mm and δ (thickness) = 2 mm) employed in the present study (*a*) alongside those airfoils used by Hassanalian et al. [2019] (*b-f*).

Thus, in the present study, we aim to investigate the effects of warming and cooling upper surface by using a simple symmetric NACA0012 airfoil. Figure 2 shows the difference between NACA0012 airfoil and those used in bio-inspired studies that include NACA2412, MH20, S5020, GOE174 and E186 [Hassanalian et al., 2019]. Thus far, GOE174 is believed to be the closest representation of the albatross wing, although E186 shows maximum improvement in performance with a warmer upper surface. There are inherent differences in the shape and structure of the geometry between the airfoil used in the present study and those used in bio-inspired research. However, investigating thermal effects on the upper surface of a basic airfoil forms the first step in developing a good understanding of the force and flow characteristics. Therefore, we performed 2-dimensional simulations on the NACA0012 airfoil in OpenFOAM using Spalart-Allmaras turbulence model to capture the dynamics of turbulence. Since birds cannot sustain temperatures as high as 400 K and as low as 200 K, we chose the warmer and cooler temperatures of the upper surface within the bounds of the practical temperature difference between the upper black and lower white wings reported in Hassanalian et al. [2019] and Rogalla et al. [2019]. The resolution of the ambiguity mentioned above will help us better understand the fundamentals of aerodynamics and prove beneficial for further design of bioinspired drones.

Numerical Simulation

The numerical simulation is based on the RANS Spalart-Allmaras method. The computation comprises of (1) geometry of the 2D NACA0012 airfoil creation; (2) conceptualizing the flow governing equations; (3) grid generation and validation of simulation model.

Geometry of the airfoil:

Figure 3 shows the essential terminologies associated with an airfoil. The leading edge is the point at the front of the airfoil with maximum curvature. Similarly, the trailing edge is the point at the back of the airfoil with maximum curvature. The chord line joins the leading and trailing edge, denoted by the letter c. The mean camber line is the locus of points midway between the upper and lower surface of the airfoil. The maximum camber is the maximum difference between the mean camber line and the chord line. Finally, AOA is the angle made by the wind direction and the chord line of the airfoil. In the body of the paper, these terms will be mentioned again, with AOA being referred in degrees throughout.

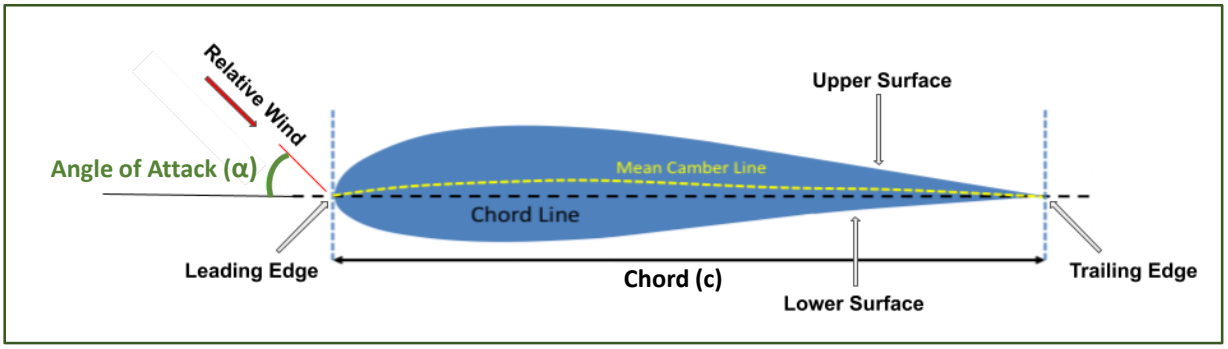

Fig. 3 Characterization of a 2D airfoil.

An airfoil is for producing lift while minimizing drag. It is reported that airfoil performance is greatly influenced by the geometries when the upper surface is warmer than the ambient and exhibits varying degrees of lift improvement and drag reduction, see Table 1 [Hassanalian et al., 2019]. Therefore, the choice of airfoil is crucial. A symmetrical 2-dimensional NACA0012 airfoil is selected in this study because of its simple geometry. The simple airfoil ensures any effects of warming the upper surface on the airfoil performance reliant on the geometry of the airfoil. It also eliminates the effects of maximum camber thickness or curves of more complex airfoils since for NACA0012 airfoil, it is essentially zero.

The geometry of the NACA0012 airfoil was created in Gmsh using Equation 4 [2D NACA 0012 Airfoil Validation]. In Equation 4, the ± in the y direction represents the symmetry of the airfoil along the x-axis. The independent x terms represent the extension of the airfoil in the x-direction (chord) and the dependent y term shows the extension of the airfoil in the y-direction (thickness), therefore, the 2D airfoil is confined in the x and y directions.

$$y = \pm\ 0.594689181 \times [0.298222773 \times x^{0.5} - 0.127125232 \times x^{1} - 0.357907906 \times x^{2} + 0.291984971 \times x^{3} - 0.105174606 \times x^{4}] \quad (4)$$

Using data from the NASA turbulence modeling resource, the airfoil is created between $x = 0$ and $x =$ 1.008930411365 (the *trailing edge* is sharp at this location). Then the airfoil is scaled down by a factor of 1.008930411365 resulting in replication of the 2D NACA0012 airfoil with $c = 1\ m$. Scaling down the airfoil in OpenFOAM by 1/50th factor gives NACA0012 airfoil under study with c = 20 mm, shown in Fig. 2*a*.

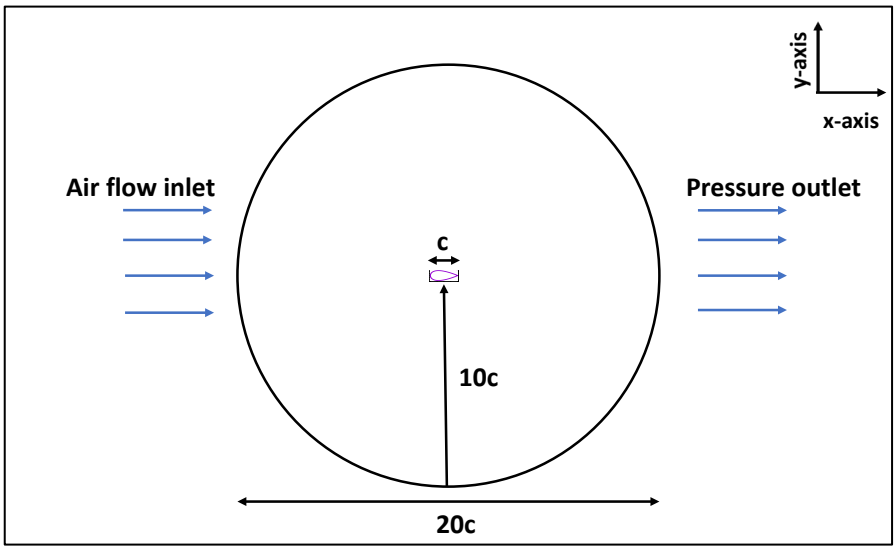

Fig. 4 Dimensions of the computational domain in terms of chord length c.

Following the convention, the chord length (c) and thickness (δ) of the airfoil are taken as the characteristic lengths in x and y-directions, respectively. Dimensions of the computational domain shown in Fig. 4 are scaled by the chord length c. The radius of the circular domain is $10c$. The airfoil is located at approximately $10c$ downward of the uniform inlet stream. The reference of the coordinate system is fixed at the center of the airfoil, corresponding to ($10c$, $10c$). The velocity of the inlet stream of air in the x-direction is set at 24 m/s, and $T_a = 300$ K. This computational domain results in a turbulent flow with $\mathrm{Re} = 3.3 \times 10^4$.

Governing Equations:

The Navier Stokes equation lies at the heart of all computational fluid dynamics simulations. Although the name Navier Stokes was initially restricted to the conservation of linear momentum, nowadays, the Navier Stokes equation is used to denote the conservation of mass, momentum, and energy altogether. Due to the broad applicability of the equation ranging from the simulation of hurricanes to blood flow in an artery, it is essential to walk through the fundamentals.

Consider an airfoil control mass (*CM*) enclosed in a control volume (*CV*) of volume (*V*), with control surface *S* in an inertial reference frame (*x, y, z*) as depicted in Fig. 5. The airfoil *CM* has a constant mass m, density ρ, and velocity $\boldsymbol{v}$. The flow field enclosed in the *CV* around the airfoil varies both in space and time. It is evident that in the absence of any mass source or sink, a region will conserve its mass locally. Therefore, the mass will remain conserved. Reynolds Transport Theorem is a general conservation law that relates *CM* conservation law to the *CV* under consideration [Gatski & Bonnet, 2009].

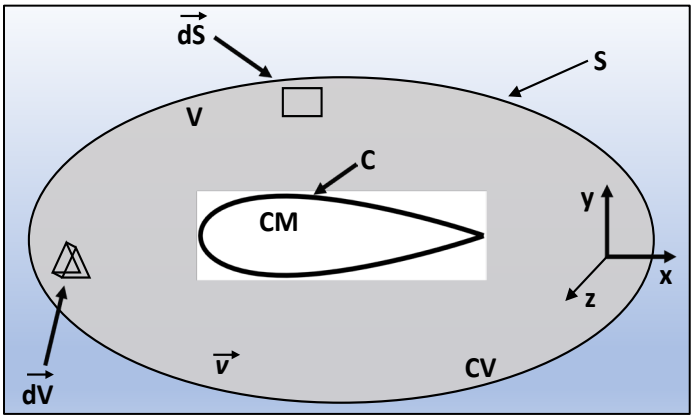

Fig. 5 Airfoil control mass *CM* within a control volume *CV* with an integration contour C defined.

Using Reynolds Transport Theorem on the Eulerian Coordinate System (*x, y, z*), the expression for mass conservation is

$$\int_{CV}^{V} \left[\frac{D\rho}{Dt} + \rho\nabla.\boldsymbol{v}\right] = 0 \tag{5}$$

Since the expression in Equation 5 is valid for an arbitrary control volume *CV*, the integral should indeed be equal to zero for it to be true for any geometry. Therefore, we can remove the integral, and the differential form of the mass conservation or continuity equation is obtained as Equation 6.

$$\frac{D\rho}{Dt} + \rho\nabla.\boldsymbol{v} = 0 \tag{6}$$

Now for a material volume of a substance, Newton's second law of motion asserts that the momentum of a specific volume can change only in the presence of a net force acting on it, which could include both surface forces ($\boldsymbol{f_s}$) and body forces ($\boldsymbol{f_b}$). Therefore, considering the *CV* in Fig. 5, its total momentum should remain conserved due to the absence of a net external force. Again, using Reynolds Transport Theorem on the *CV* for momentum conservation, the expression for momentum conservation becomes,

$$\int_{CV}^{V} \left[\frac{\partial[\rho\boldsymbol{v}]}{\partial t} + \nabla.\rho\boldsymbol{v}\boldsymbol{v} - \boldsymbol{f}\right] dV = 0 \tag{7}$$

Here, $\boldsymbol{f} = \boldsymbol{f_s} + \boldsymbol{f_b}$ and *CV* is an arbitrary geometry in space that contains *CM*. For Equation 7 to be true

for any arbitrary geometry, the integral must indeed be equivalent to zero and the momentum equation in differential form is represented below,

$$\frac{\partial[\rho \boldsymbol{v}]}{\partial t} + \nabla . \rho \boldsymbol{v}\boldsymbol{v} - \boldsymbol{f} = 0 \tag{8}$$

It is worth mentioning that $\boldsymbol{f_s}$ and $\boldsymbol{f_b}$ terms can further be expanded to reveal a more comprehensive version of Eq. 8. However, such derivations are beyond the scope of the presented study, and further details can be found in existing literature [Anderson., 2017; Moukalled et al., 2016].

The energy equation is not coupled with the mass and momentum equation for incompressible flows. Instead, it is solved independently after obtaining velocity and pressure fields from the mass and momentum equations. However, for compressible flows, density and viscosity no longer remain constant, and their effects need to be accounted for with variations in temperature simultaneously. Consider the random motion of gas molecules in a closed container. As temperature increases, the gas molecules gain energy, and their random motion increases, leading to viscosity and density changes. To account for such changes, ***Sutherland's law*** is used in this work to relate the dynamic viscosity μ with temperature [Sutherland, 1893].

Furthermore, for a closed, isolated system, the sum of all forms of energy remains constant. In Figure 5, the *CV* has a total energy per unit mass of e. If $\dot{q}_v$ represents the rate of heat source/sink within the material volume per unit volume and $\dot{\boldsymbol{q}}_{\boldsymbol{s}}$ is the rate of heat transfer per unit area across the surface area of the material element, then invoking the First Law of Thermodynamics, the governing energy equation becomes,

$$\frac{\partial(\rho e)}{\partial t} + \nabla.[\rho v e] = -\nabla.\dot{\boldsymbol{q}}_{\boldsymbol{s}} - \nabla.[p\boldsymbol{v}] + \nabla.[\boldsymbol{\tau}.\boldsymbol{v}] + \boldsymbol{f_b}.\boldsymbol{v} + \dot{q}_v \tag{9}$$

Here, p is the pressure distribution around the *CV*. Equation 9 can be written in terms of specific internal energy, specific total enthalpy, or temperature.

It comes as no surprise that when temperature changes, the density of gas changes. The nature of density variation plays an important role in solving Equations (5-9). If the molecules involved are that of an ideal gas with pressure p and R is the gas constant, then the relationship between density and temperature can be represented using the ideal gas equation,

$$\rho = \frac{p}{RT} \tag{10}$$

While deriving the equation of motions, no mention was made as to whether the flow is laminar or turbulent. The laminar flow is stable and streamlined, whereas turbulent flow is random and more diffusive, causing rapid inter-mixing and formation of eddies. Due to the highly random fluctuations, a deterministic approach is not possible for turbulent flow solutions. Thus, Reynolds came forward with an averaging concept named Reynolds Averaged Navier – Stokes (RANS). Through the concept of RANS, all flow quantities are expressed as the sum of mean and fluctuating components. Therefore, in all the equations mentioned above, instead of just considering steady flow quantities, their time-averaged terms must be substituted (consisting of mean and fluctuating components) to account for the turbulence generated. The step is crucial since the simulations performed in this study at $\mathrm{Re} = 3.3 \times 10^4$ are under turbulent flow conditions.

Simulation, Verification, and Validation:

The system closure was realized using the RANS ***Spalart-Allmaras*** [Allmaras, 1992] model. The one equation Spalart-Allmaras model is used because, unlike other algebraic models [Baldwin et al., 1978; Johnson & King, 1985] and one equation models [Bradshaw et al., 1967; Nee & Kovasznay, 1969; Thomas & Salas, 1986], the Spalart-Allmaras model is local. The locality means that the model is compatible with grids of any structure (structured and unstructured) and Navier Stokes solvers in 2D and 3D. Then the system of steady-state compressible Navier Stokes equations is solved using ***rhoSimpleFoam*** solver, and the variable fluid properties are simulated using the ***thermophysical*** library of OpenFOAM.

The mesh around the geometry of the 2D NACA0012 airfoil is generated using Gmsh and converted to an OpenFOAM environment. The entire domain mesh and zoom-in of the finer mesh near the airfoil are illustrated in Fig. 6. The airfoil is then split into the upper and lower surface patches to implement temperatures warmer and cooler than the ambient.

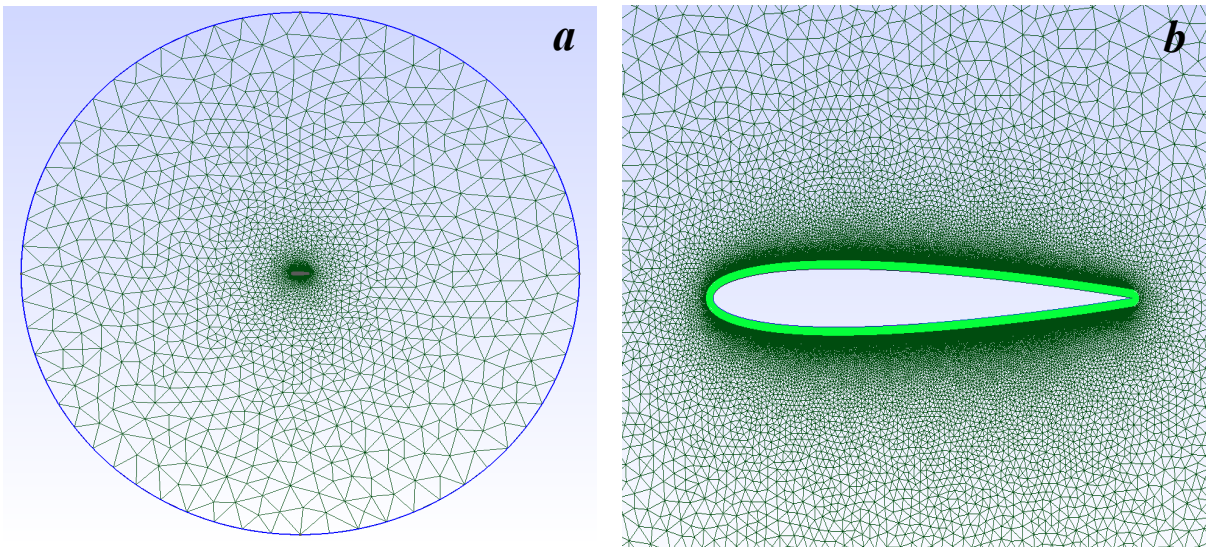

Fig. 6 Domain mesh around the 2-D airfoil: (*a*) whole domain and the refinement boxes; (*b*) zoom-in at the airfoil surroundings.

To begin, mesh independence and convergence studies are carried out at Re = 3.3×10^4 with no surface heating or cooling at a Mach Number (Ma) of 0.0725 and $T_a = 300$ K. Figure 7*a* shows the variation of C_L at four AOA values and its convergence with mesh refinement. While using a fine mesh, with 15×10^4 nodes and beyond, no significant change in the solution is obtained at all AOA values. However, for meshes with less than 2.5×10^4 nodes, the solution diverges. Figure 7*b* shows the variation of C_D at the four studied AOA values. A coarse mesh overpredicts the value of the drag coefficient significantly. The overprediction decreases rapidly with increasing number of elements, and the asymptotic value reached when the number of nodes is 15×10^4. Thus, a mesh consisting of 15×10^4 nodes, 130970 quadrangles, and 35364 triangles was chosen for all the further simulations performed.

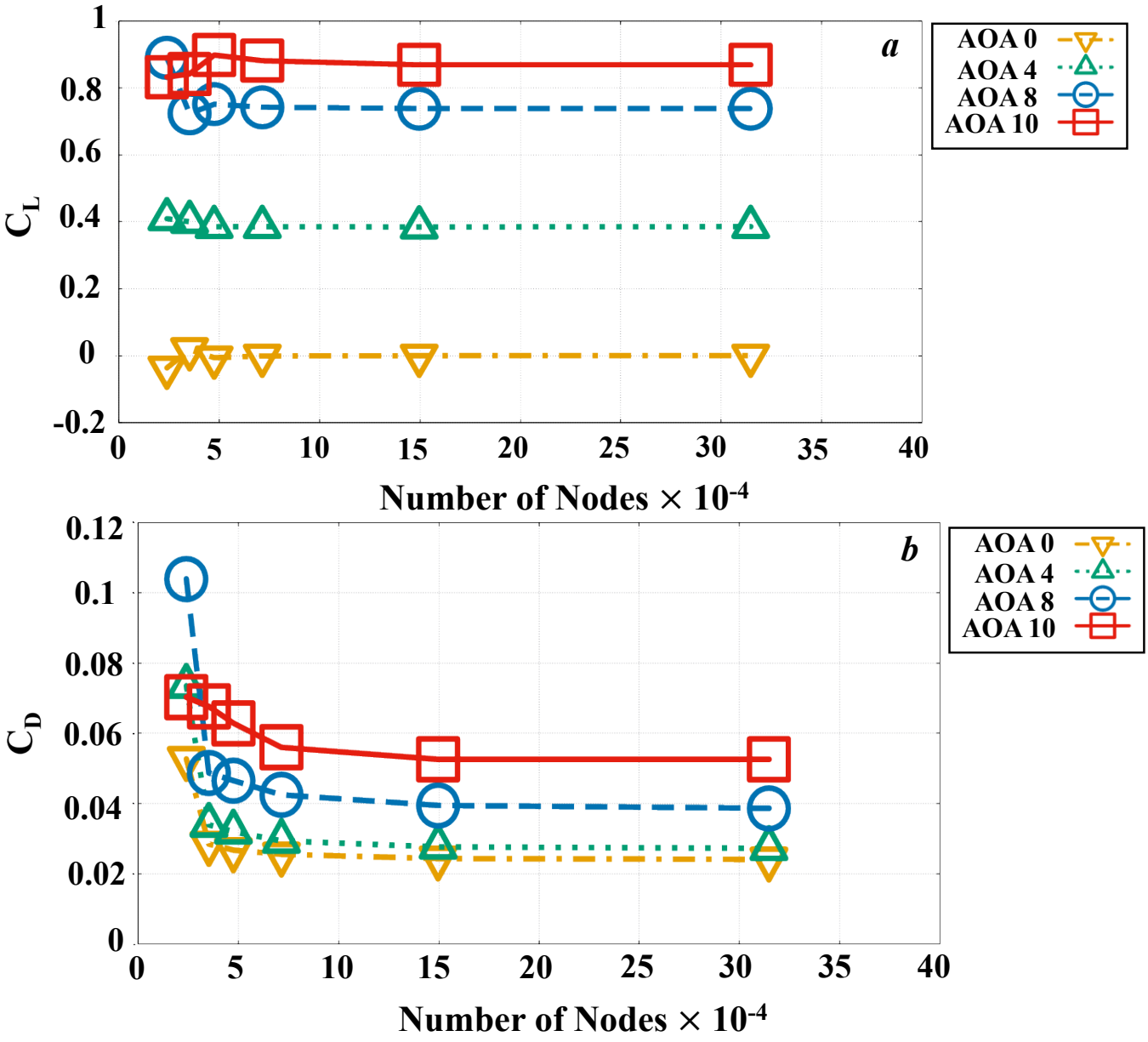

Fig. 7 Grid independency results: The effect of number of nodes on (*a*) C_L and (*b*) C_D are obtained at Ma = 0.0725, Re $= 3.3 \times 10^4$, and T_a $= 300$ K.

To validate the code, an airflow with Ma = 0.0725, at pressure of 1 atm, and $T_a = 300$ K is set up in the airfoil domain and simulated. The airfoil's upper and lower surfaces are maintained at a temperature of 300 K and the flow Re $= 3.3 \times 10^4$.

To facilitate a generalized expression for easier interpretation, the temperature difference is normalized as:

$$\frac{\Delta T}{T_a} = \frac{(Upper\ surface\ temperature - Lower\ surface\ temperature)}{Ambient\ temperature} \tag{11}$$

Figure 8*a* shows the variation of C_L with AOA at Re $= 3.3 \times 10^4$, Ma = 0.0725 and T_a = 300 K. The upper surface of the airfoil is held at a constant temperature of 300 K. The corresponding C_L/C_D ratio is plotted as a function of AOA in Fig. 8*b*, and the results are validated with data obtained by Kim et al. [2003]. The presented results are in good agreement. While both studies employ the Spalart-Allmaras model for simulating turbulence, the grid size and shape are different. In our study, a circular control surface is used whereas a parabolic control surface was deployed by Kim et al. [2003]. Furthermore, the present simulations are performed in OpenFOAM, while Kim et al. [2003] utilized FLUENT.

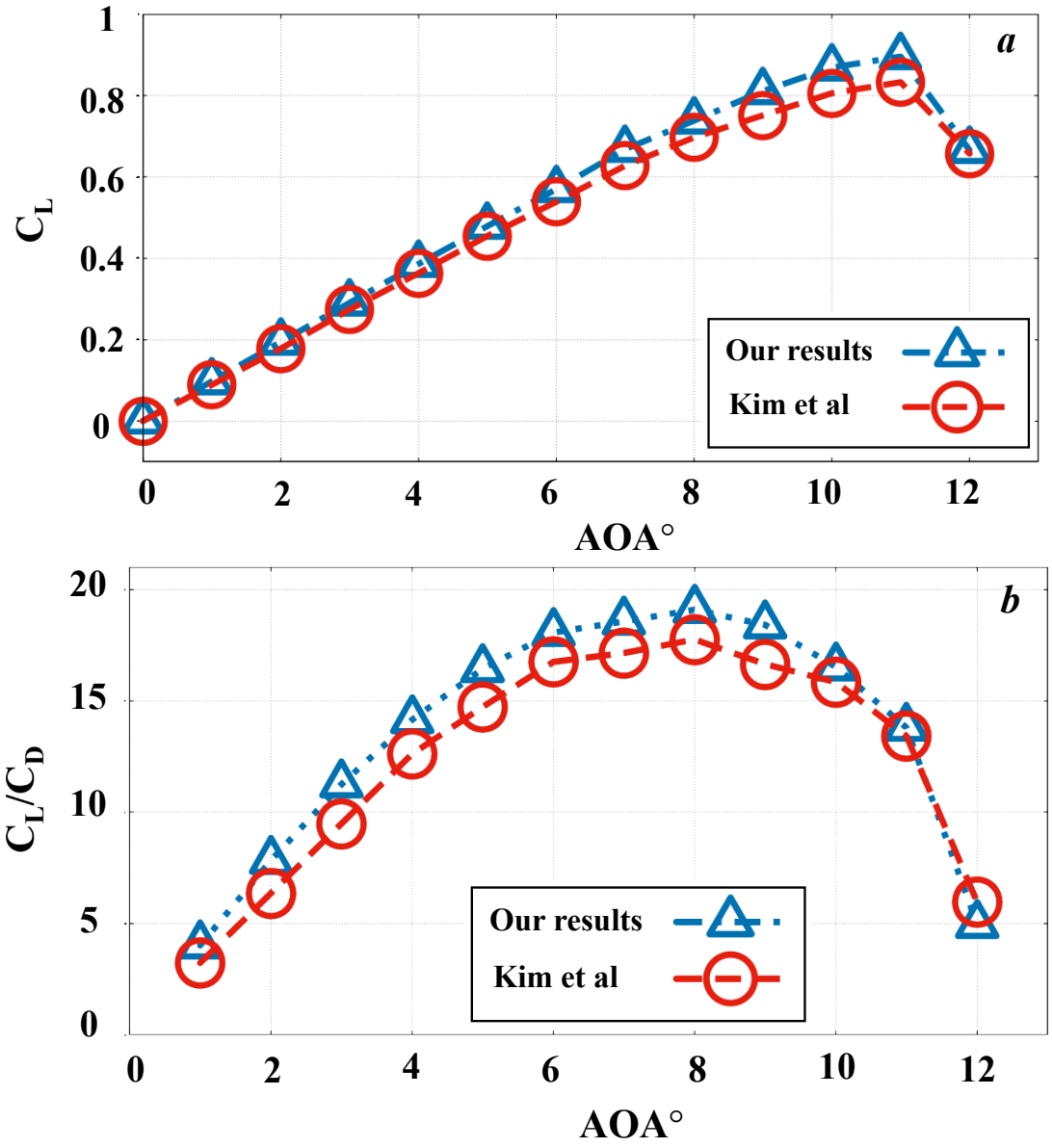

Fig. 8 Validation of present work: The effect of AOA on (*a*) C_L and (*b*) C_L/C_D of NACA0012 airfoil at Ma = 0.0725, Re $= 3.3 \times 10^4$, and T_a = 300 K.

Results and Discussion

Previous research [Hassanalian et al. 2019; Rogalla et al. 2019] has shown that the black-colored wings of birds, such as the albatross, warm up faster than the white-colored ones. The differing solar absorptivity of black and white colors causes uneven warming. The uneven warming sets up a temperature difference between the top and bottom surfaces of the wings. Their study revealed a temperature difference of almost 30°C between the top black and white bottom wing. Thus, a temperature difference of 30 K is used in the present study to investigate warmer and cooler than the ambient upper surface on the performance of NACA0012 airfoil.

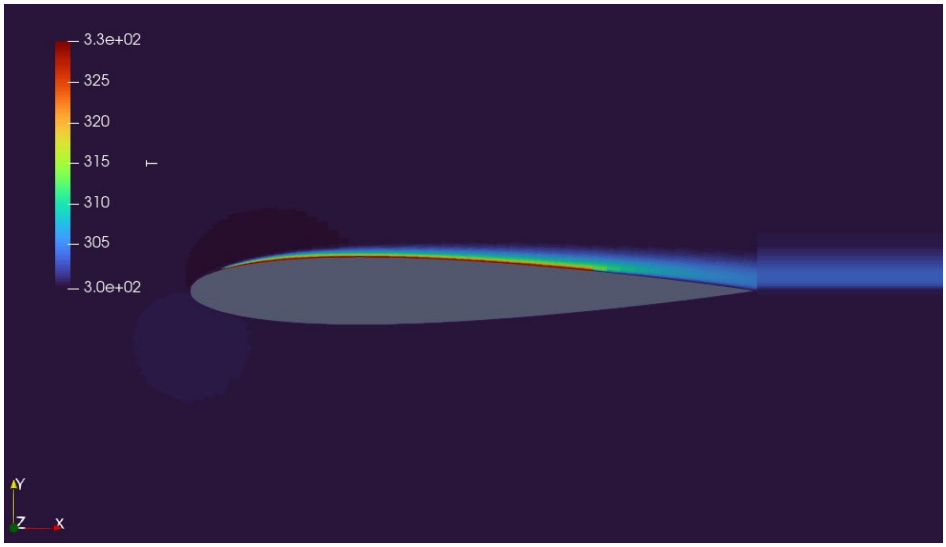

Fig. 9 Convective heat transfer from the warm upper surface of the airfoil (T_u = 330 K) to the ambient (T_a = 300 K).

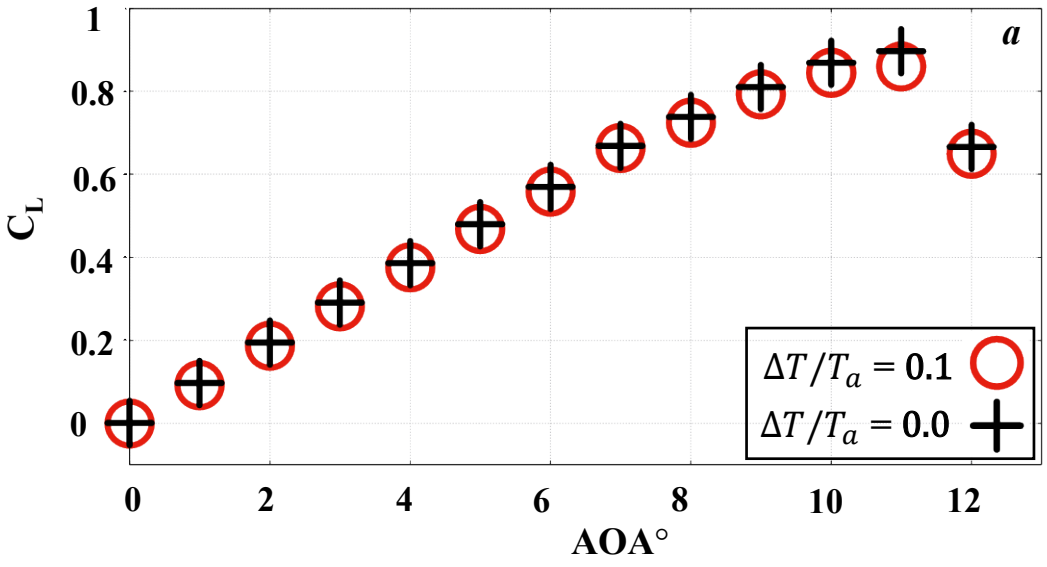

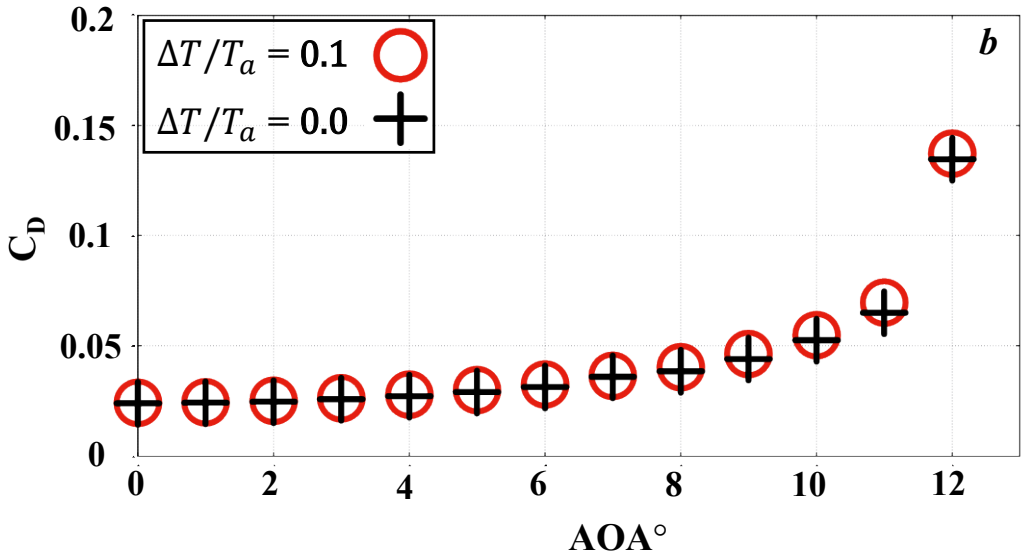

Fig. 10 The effects of heating on lift and drag at Re $= 3.3 \times 10^4$ and Ma = 0.0725: (a) C_L vs. AOA; (b) C_D vs. AOA.

The upper surface of the NACA0012 airfoil, at $T_a = 300$ K, Re $= 3.3 \times 10^4$ and Ma = 0.0725, is warmed to a uniform temperature of 330 K ($\Delta T = 30\ K\ and\ \frac{\Delta T}{T_a} = 0.1$). The surface temperatures being fixed, we do not consider heat transfer in the solid airfoil via conduction (from the hot to cold surface). Convective heat transfer, shown in Fig. 9, is modelled using the rhoSimpleFoam solver and thermophysical library of OpenFOAM. The force coefficients are calculated when the upper surface temperature is the same and warmer than the ambient. The results, presented in Fig. 10, reveal that C_L decreases, whereas C_D increases when the upper surface is warmer for all studied AOA values. The effect of a warmer upper surface is more pronounced at higher AOA values, especially when AOA = 11°. A decrease in C_L value from 0.896 to 0.860, and an increase in C_D value from 0.065 to 0.070 was obtained. It corresponds to a drop in C_L/C_D value from 13.79 to 12.35, as shown in Fig. 11.

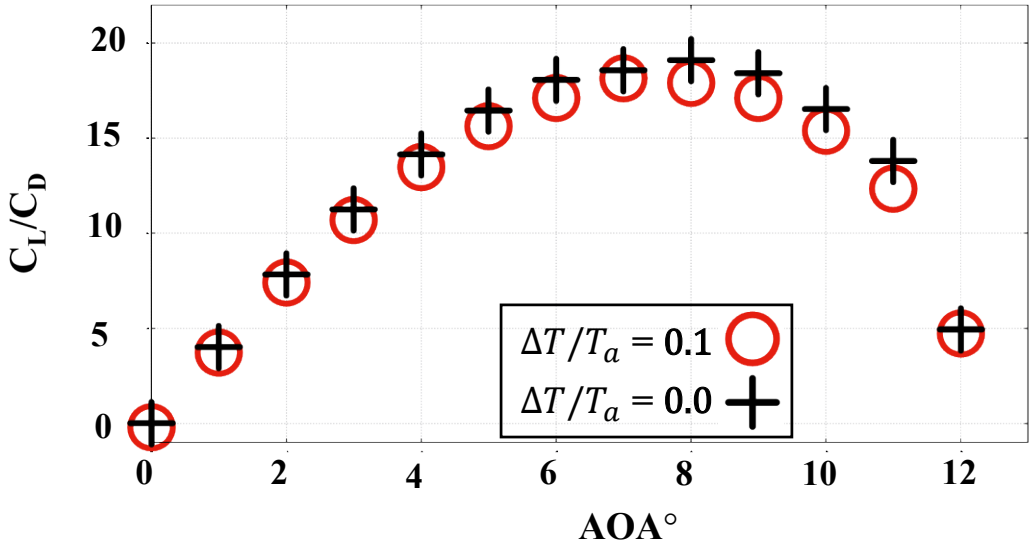

Fig. 11 The effect of heating upper surface on C_L/C_D vs. AOA at Re $= 3.3 \times 10^4$, $\frac{\Delta T}{T_a} = 0.1$, $\frac{\Delta T}{T_a} = 0.0$ and Ma = 0.0725.

To uncover the underlying physics behind the observed changes in C_L and C_D, the pressure and wall-shear stress values on the airfoil's upper surface are plotted against the geometry of the airfoil to visualize the distribution. The pressure and wall-shear stress are plotted for the largest observed changes in lift and drag at AOA = 11°.

As shown in Fig. 12, the value of pressure for the $\frac{\Delta T}{T_a} = 0.1$ case is larger when compared to the reference $\frac{\Delta T}{T_a} = 0$ case. The increase is pronounced near the leading edge of the airfoil, with the maximum increase occurring at approximately $x/c = 0.25$ (the leading edge is at $x/c = 0$ and $c = 20\,mm$). The pressure difference reduces as we move along the airfoil's chord towards the trailing edge, and it attains almost same pressure as the airfoil's upper surface for the no-heating case.

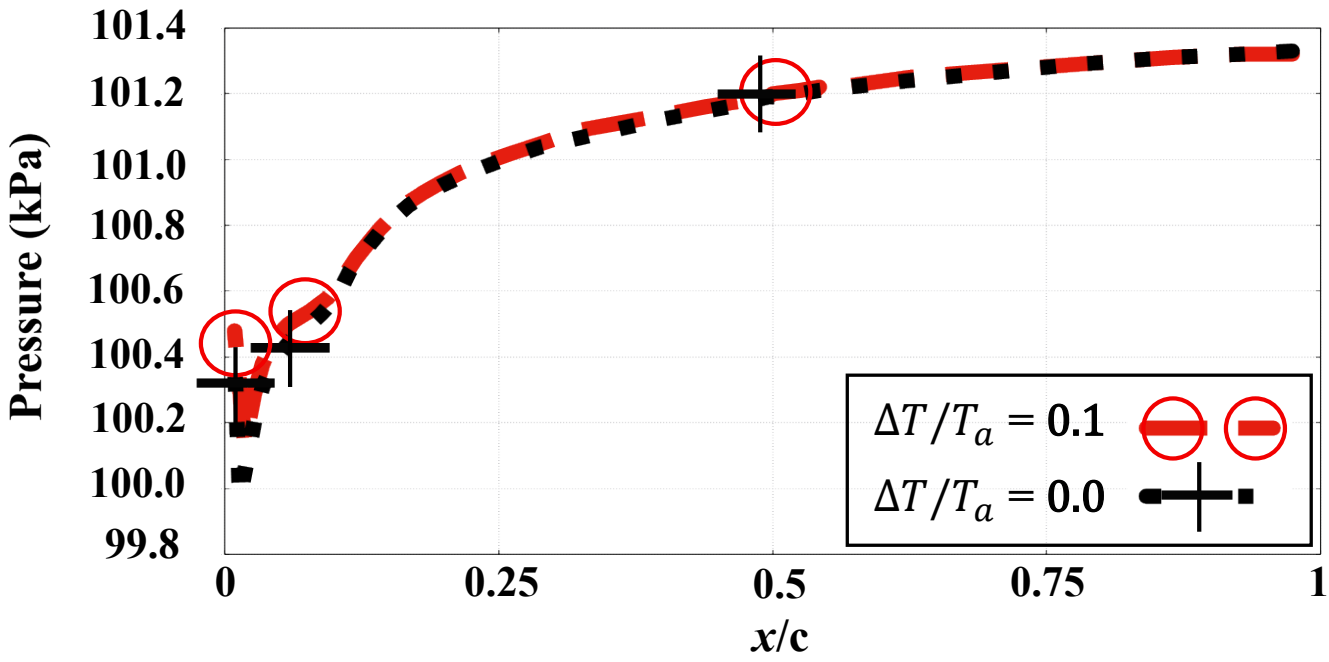

Fig. 12 Pressure (kPa) along the upper surface of the airfoil at AOA = 11°.

Furthermore, a similar trend is observed by the wall shear stress as in the case of pressure shown in Fig. 13. A significant change between warmer and normal upper surface of the airfoil peaks around the leading edge of the airfoil. The difference is reduced as we move towards the airfoil's trailing edge. A noteworthy feature here is that the wall shear stress increases from 0.83 Pa to 1.40 Pa near the airfoil's leading edge. The exact location corresponds to approximately $x/c = 0.25$. The present results show that wall shear stress at the upper surface of the airfoil increase with warmer temperatures than ambient. The reason being that for air, both the dynamic and kinematic viscosity increase with temperature. As a result, the shear increases which slows down the fluid flow (Figure 19) and increases the pressure.

The present simulations suggest that upper surface heating of the NACA0012 airfoil causes rise in drag and reduction in the lift by increasing the pressure mainly around the nose region of the airfoil. The increased pressure pushes the airfoil downwards and results in reduced lift. On the other hand, the increased value of wall shear stress in the x-direction (the air flow direction) and the increased viscosity negatively affects the drag.

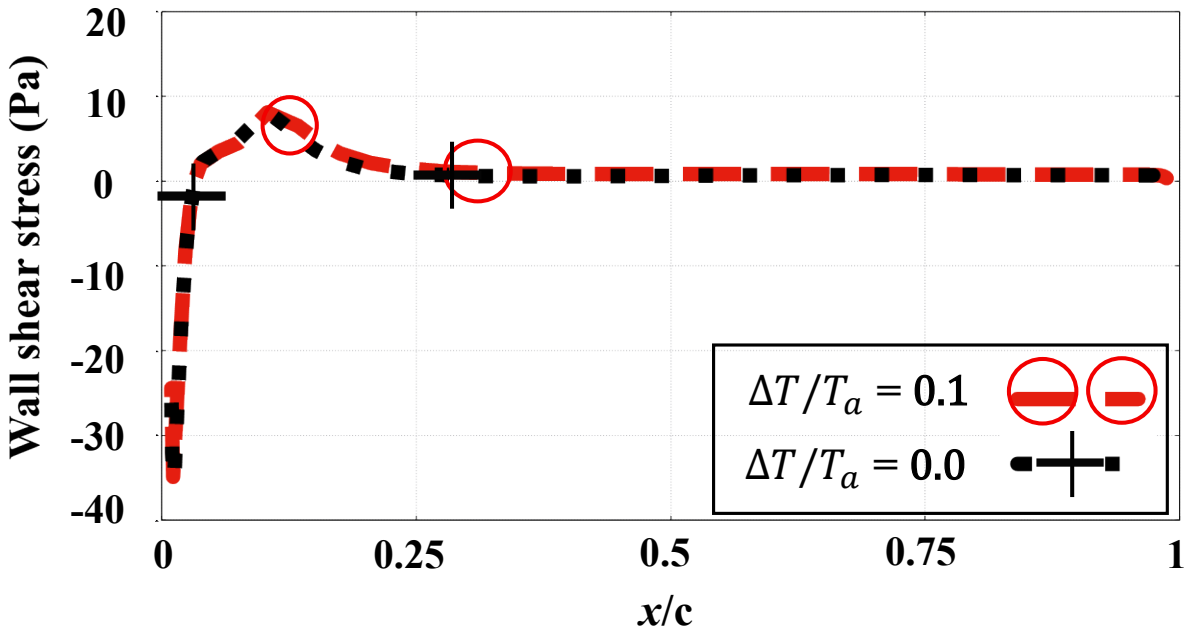

Fig. 13 Wall shear stress (Pa) along the upper surface of the airfoil at AOA = 11°.

The results of our study contradict the concept of birds utilizing surface heating to optimize their flight efficiency. Since the warmer upper surface shows a negative effect, considering a cooler upper surface seems the next appropriate choice. For this purpose, the upper surface of the NACA0012 airfoil was cooled to 270 K ($\Delta T = -30\ K\ and\ \frac{\Delta T}{T_a} = -0.1$) and the simulations were repeated under the same flow conditions. Like the case of warming, for cooling, heat transfer from the cooler airfoil surface to the warmer one via conduction in the solid airfoil is not taken into consideration. Convective heat transfer, shown in Fig. 14, is modelled similarly using the rhoSimpleFoam solver and thermophysical library of OpenFOAM. The effect of a cooler upper surface on the values of C_L and C_D is presented in Fig. 15. The lift increases, while the drag reduces, and the maximum increase in C_L/C_D occurs at AOA = 11°. The C_L increases from 0.896 to 0.933, whereas C_D decreases from 0.065 to 0.061. The corresponding value of C_L/C_D increases from 13.8 to 15.3, as shown in Fig. 16.

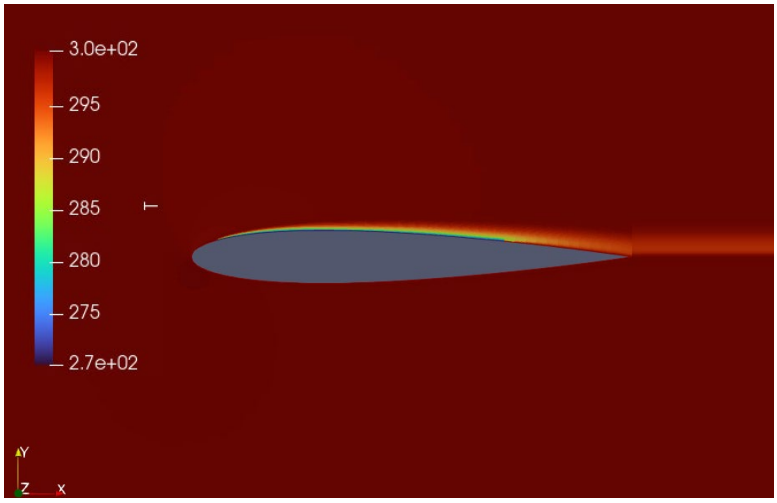

Fig. 14 Convective heat transfer from the cool upper surface of the airfoil (T_u = 270 K) to the ambient (T_a = 300 K).

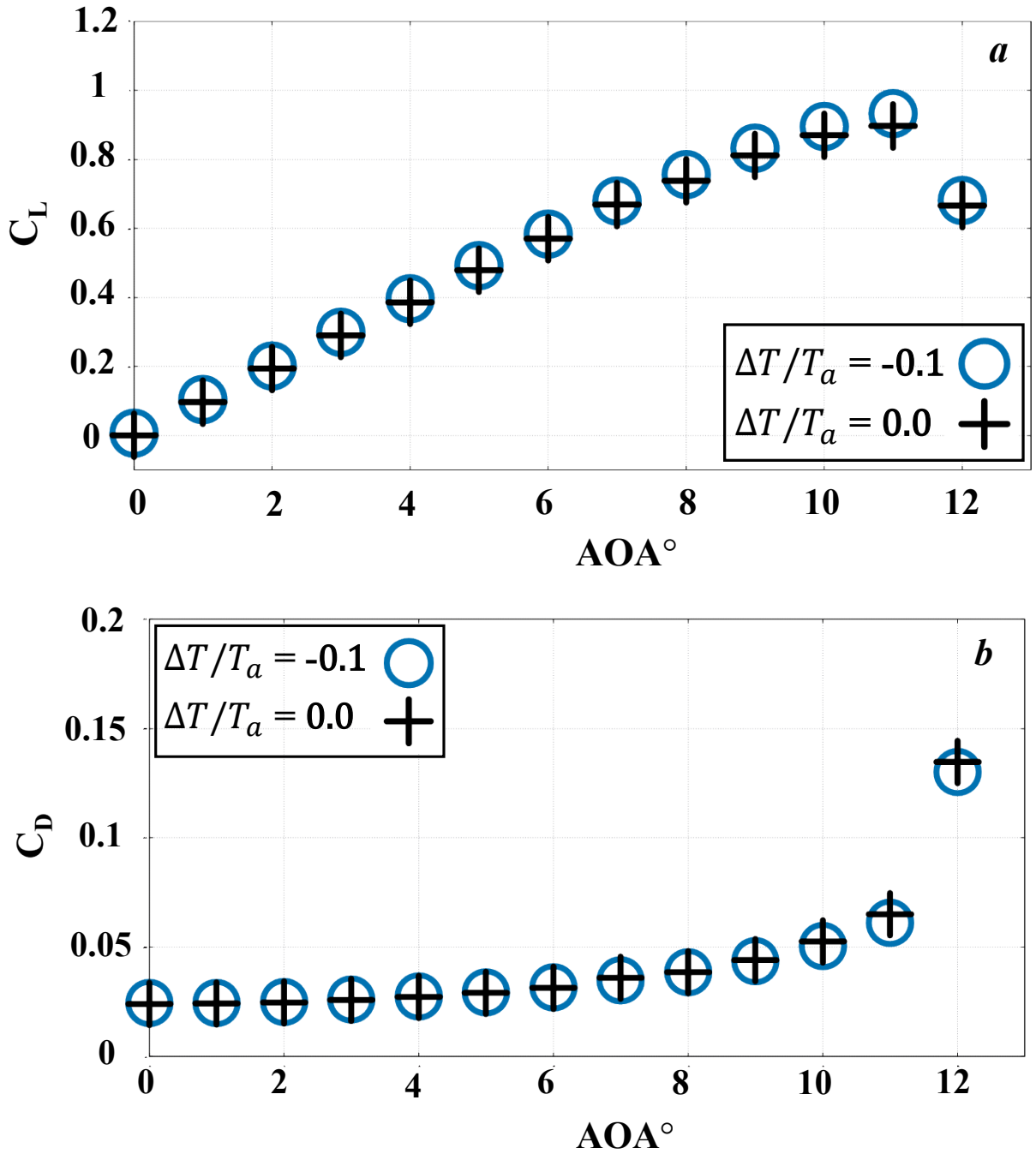

Fig. 15 The effect of cooling on lift and drag: (*a*) Comparison of C_L vs. AOA: (*b*) Comparison of C_D vs. AOA.

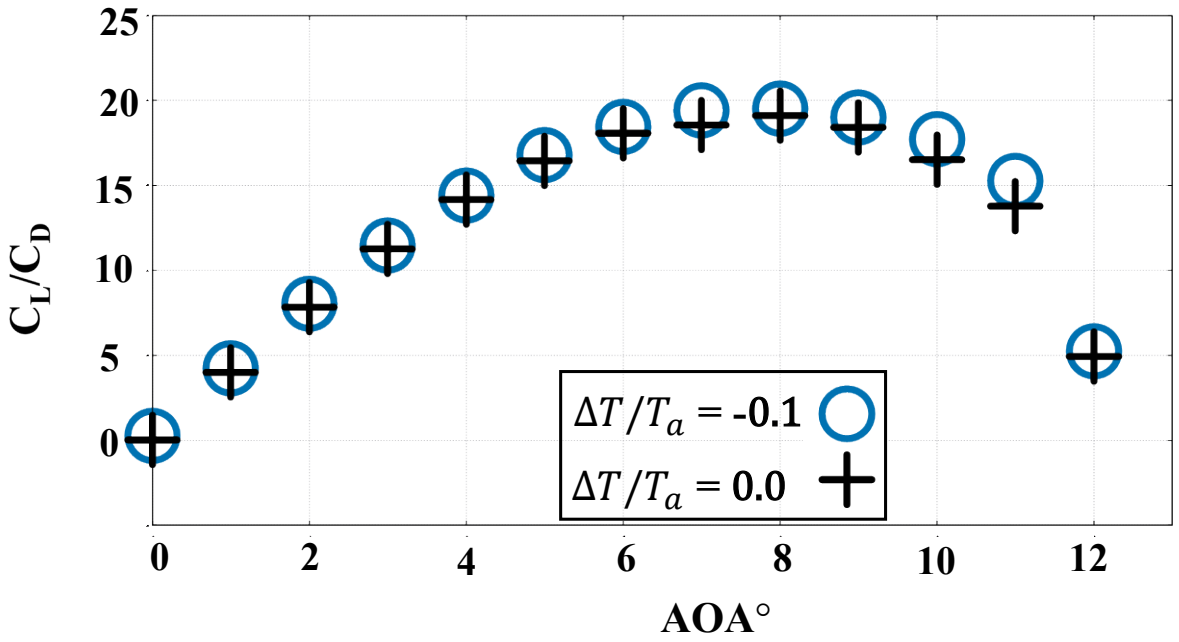

Fig. 16 The effect of cooling on C_L/C_D vs. AOA.

As shown in Fig. 17, the value of pressure for the $\frac{\Delta T}{T_a} = -0.1$ case is lower compared to the reference $\frac{\Delta T}{T_a} = 0$ case. It is the front end of the airfoil that becomes the most susceptible to change with a cooler upper surface. As we move towards the trailing edge, the pressure evens out and becomes almost like the reference $\frac{\Delta T}{T_a} = 0$ case.

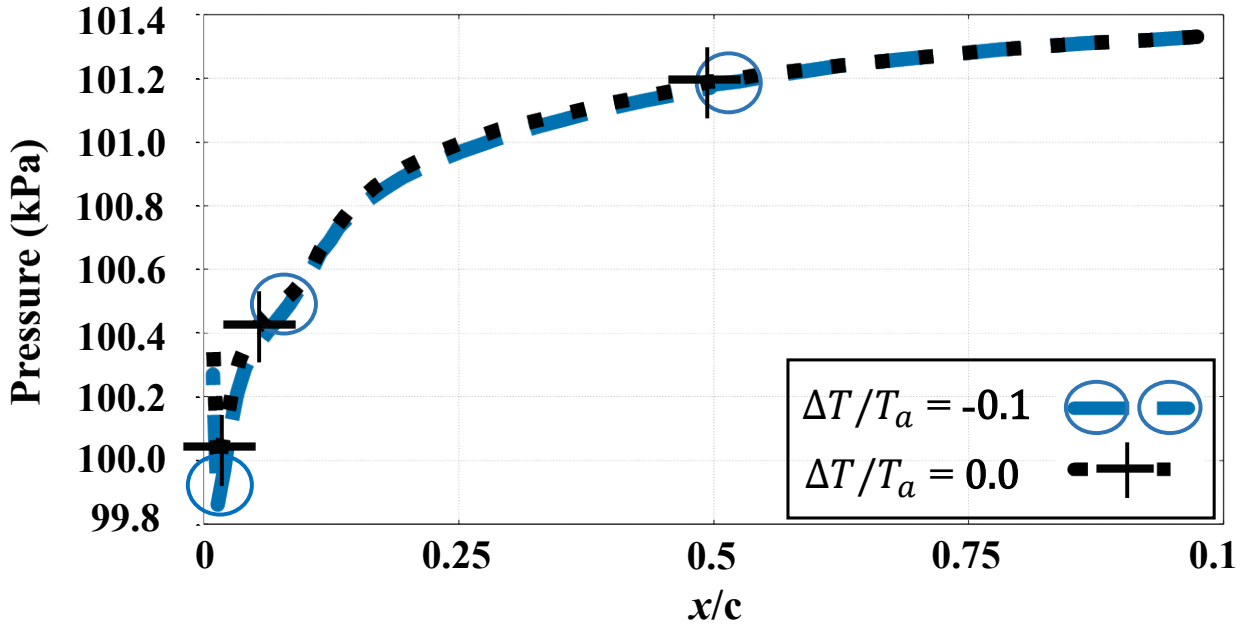

Fig. 17 Pressure (kPa) along the upper surface of the airfoil at AOA = 11°.

The wall shear stress in the x-direction decreases when the upper surface is cooled; compare $\frac{\Delta T}{T_a} = -0.1$ case with the reference $\frac{\Delta T}{T_a} = 0.0$ case in Fig. 18. The value decreases from 0.83 Pa to 0.35 Pa at $x/c = 0.25$. The decrease starts close to airfoil's leading edge and as we move towards the trailing edge, the deviation of wall shear from $\frac{\Delta T}{T_a} = 0.0$ case becomes negligible.

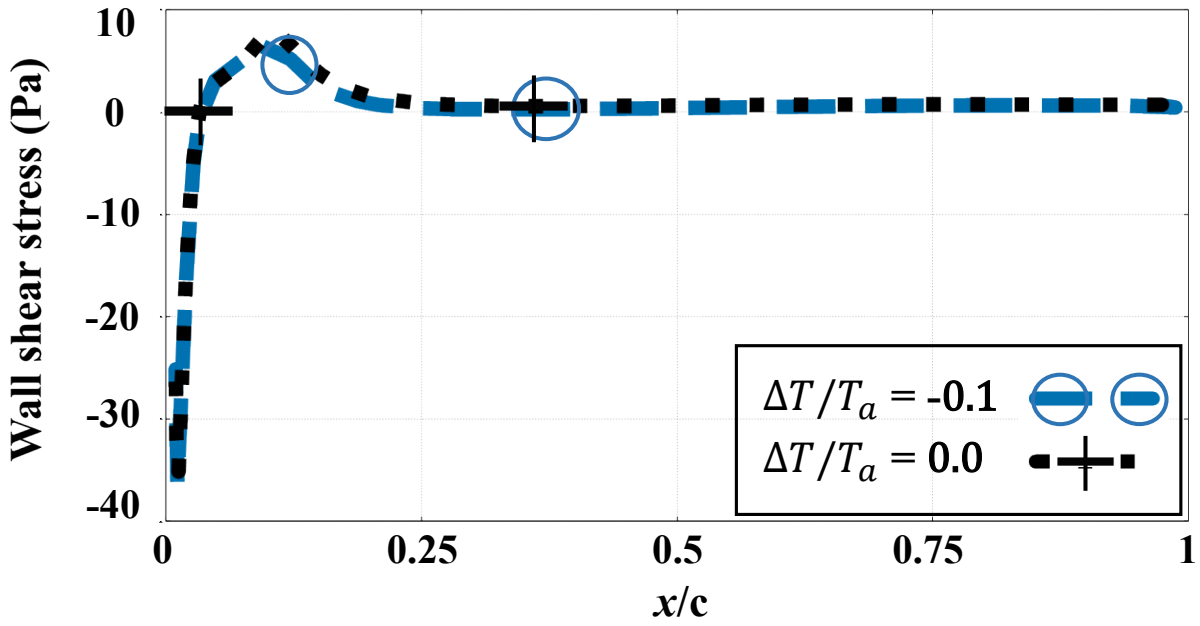

Fig. 18 Wall shear stress (Pa) along the upper surface of the airfoil at AOA = 11°.

The reduced pressure creates the necessary pressure difference near the airfoil's leading edge to increase the lift coefficient in the y-direction. At the same time, the reduced wall shear stress in the x-direction reduces the drag coefficient. The reason being with decreasing temperature, the viscosity decreases. As a result, the local velocity near the leading edge of the airfoil increases, causing the pressure to decrease. Figure 19 highlights the increase in velocity on cooling near the leading edge when compared to the warmer case. A combination of these factors makes upper surface cooling a better alternative to improve the flight dynamics of the NACA0012 airfoil.

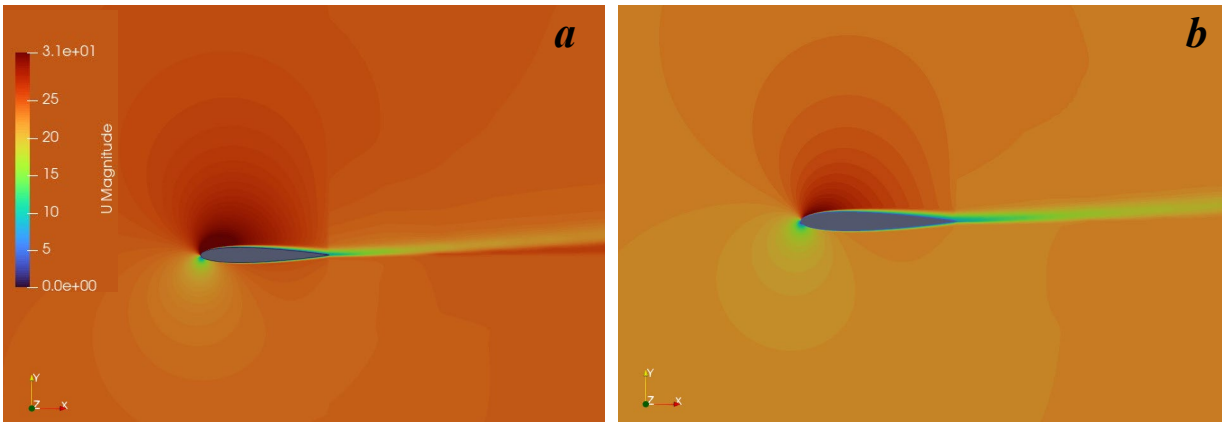

Fig. 19 Velocity distribution around the airfoil: (*a*) $\frac{\Delta T}{T_a} = -0.1$, (*b*) $\frac{\Delta T}{T_a} = 0.1$

Conclusions

Study conducted by Hassanalian et al. [2019] highlights improvement in aerodynamic performance using upper surface heating. However, similar studies conducted on a NACA0012 airfoil have revealed improvement in performance with upper surface cooling [Bekka et al., 2009; Hinz et al., 2013; Kim et al., 2003; Samiee et al., 2018]. The present study transpires from the above existing contrast in literature. We investigated the effects of temperatures warmer and cooler than the ambient on the aerodynamic performance of a simple 2D NACA0012 airfoil.

To understand the effects of such thermal camber, 2D numerical simulations were performed using OpenFOAM to understand the aerodynamic performance of NACA0012 airfoil subjected to turbulent flow conditions ($\mathrm{Re} = 3.3 \times 10^4$) at $T_a = 300$ K, $T_u = 300 \pm 30$ K, p = 1 atm and Ma = 0.0725. The major findings of the study are summarized as follows:

When the upper surface of the NACA0012 airfoil is kept at uniform temperature warmer than the ambient ($\frac{\Delta T}{T_a} = 0.1$), the aerodynamic performance of the airfoil suffers negatively. The C_L value decreases from 0.896 to 0.860 (4% reduction in lift) and the C_D value increases from 0.065 to 0.070 (8% increase in drag). Overall, the maximum magnitude of reduced performance was observed at AOA 11° with $C_L/\ C_D$ value decreasing from 13.79 to 12.35 (10% drop in performance).

Since warmer temperatures showed a negative effect, the upper surface of the airfoil was further tested at uniform temperature cooler than the ambient ($\frac{\Delta T}{T_a} = -0.1$) and it improved the aerodynamic performance. The C_L value increased from 0.896 to 0.933 (4% rise in lift) and the C_D value decreased from 0.065 to 0.061 (6% reduction in drag). Again, the maximum enhancement in performance was observed at AOA 11° with $C_L/\ C_D$ value increasing from 13.8 to 15.3 (11% improvement).

The reported 11% increase or 10% decrease have been obtained at an AOA of 11° at upper surface temperate of 330 K and 270 K, respectively, with $T_a = 300$ K, p = 1 atm and Ma = 0.0725.

Contrary to the existing bioinspired studies on upper surface heating of airfoils, our study finds that cooler upper surface of the NACA0012 airfoil than the ambient improves the aerodynamic performance. The improvement occurs due to the reduced pressure and wall shear stress that increase the lift and reduce the drag forces respectively.

It appears that Hassanalian et al [2019] is contrary to other studies including our, which is an anomaly. It is important to note that the wings of birds are three dimensional and have intelligently designed morphology, whereas a simple, smooth, two-dimensional airfoil has been simulated in studies such as ours. It should be noted that although the NACA0012 airfoil does not mimic the wings of birds exactly, the present study lays the foundation of analyzing thermal camber in airfoils inspired from birds like albatross.

Further modifications can be added to the geometry of the NACA0012 airfoil to resemble in much more depth, the actual wings of birds. 3D simulations form the next step of the presented study, to capture the vortices around the airfoil and its change with further bioinspired studies.

Acknowledgements

This work is made possible by MITACS Globalink Research Internship Programme Canada. The lead author would like to thank MITACS for providing the enriching opportunity to conduct research at the University of Windsor.

References

Allmaras, S. R. (1992). A One-Equation Turbulence Model for Aerodynamic Flows. AIAA-92-G439.

Anderson, J. (2017). Fundamentals of Aerodynamics. McGraw-Hill Education, 2 Penn Plaza, New York, NY 10121.

Baldwin, B. S., Lomax, H., (1978). Thin Layer Approximation and Algebraic Model for Separated Turbulent Flows. AIAA 16th Aerospace Sciences Meeting (16-18 January, Huntsville, AL, U.S.A).

Balestrieri, E., Daponte, P., De Vito, L., Lamonaca, F. (2021). Sensors and measurements for unmanned systems: An overview. In Sensors (Vol. 21, Issue 4, pp. 1–27).

Bekka, N., Bessaïh, R., Sellam, M., Chpoun, A. (2009). Numerical study of heat transfer around the small-scale airfoil using various turbulence models. Numerical Heat Transfer; Part A: Applications, (Vol. 56, Issue 12, pp. 946–969).

Bradshaw, P., Ferriss, D. H., Atwell, N. P. (1967). Calculation of boundary-layer development using the turbulent energy equation. Journal of Fluid Mechanics, (Vol. 28, Issue 3, pp. 593–616).

Bushnell, D. M., Moore, K. J. (1991). Drag Reduction in Nature. Annu. Rev. Fluid Mech (Vol. 23, pp. 65-79).

Coyle, E. D., Simmons, R. A. (2014). Understanding the Global Energy Crisis. Purdue University Press Books, West Lafayette, 2014-03-01.

Floreano, D., Wood, R. J. (2015). Science, technology, and the future of small autonomous drones. In Nature (Vol. 521, Issue 7553, pp. 460–466). Nature Publishing Group.

Gatski, T. B., Bonnet, J.-P. (2009). Kinematics, thermodynamics, and fluid transport properties. Compressibility, Turbulence and High-Speed Flow, pp. 1–19.

Hassanalian, M., Abdelmoula, H., Ayed, S. ben, Abdelkefi, A. (2017). Thermal impact of migrating birds' wing color on their flight performance: Possibility of new generation of biologically inspired drones. Journal of Thermal Biology, 66, 27–32.

Hassanalian, M., Ayed, S. ben, Ali, M., Houde, P., Hocut, C., Abdelkefi, A. (2018). Insights on the thermal impacts of wing colorization of migrating birds on their skin friction drag and the choice of their flight route. Journal of Thermal Biology, 72, 81–93.

Hassanalian, M., Pellerito, V., Sedaghat, A., Sabri, F., Borvayeh, L., Sadeghi, S. (2019). Aerodynamics loads variations of wings with novel heating of top surface: Bioinspiration and experimental study. Experimental Thermal and Fluid Science, 109.

Hedenström, A. (2002). Aerodynamics, evolution, and ecology of avian flight. In Trends in Ecology & Evolution (Vol. 17, Issue 9 pp. 415-422).

Hinz, D. F., Alighanbari, H., Breitsamter, C. (2013). Influence of heat transfer on the aerodynamic performance of a plunging and pitching NACA0012 airfoil at low Reynolds numbers. Journal of Fluids and Structures, 37, 88–99.

Johnson, D. A., King, L. S. (1985). A mathematically simple turbulence closure model for attached and separated turbulent boundary layers. AIAA Journal, 23(11), 1684–1692.

Kim, J., Rusak, Z., Koratkar, N. (2003). Small-scale airfoil aerodynamic efficiency improvement by surface temperature and heat transfer. AIAA Journal, 41(11), 2105–2113.

Longo, J. M. A., Radespiel, R. (1995). Numerical Simulation of Heat Transfer Effects on 2-D Steady Subsonic Flows. 26th AIAA Fluid Dynamics Conference, AIAA 95-2298.

Moukalled, F., Mangani, L., Darwish, M. (2016). Fluid Mechanics and Its Applications. The Finite Volume Method in Computational Fluid Dynamics. (Vol. 113, Springer International Publishing Switzerland)

NACA 0012 2D Airfoil Validation. From https://turbmodels.larc.nasa.gov/naca0012_val.html

Nee, V. W., Kovasznay, L. S. G. (1969). Simple phenomenological theory of turbulent shear flows. Physics of Fluids, 12(3), 473–484.

Norton, D. J., Macha, J. M., Young, J. C. (1973). Surface temperature effect on subsonic stall. Journal of Spacecraft and Rockets, 10(9), 581–587.

Ribeiro, D. G., Bravo-Mosquera, P. D., Muñoz, H. D. C. (2019). Heat transfer effects on aerodynamic performance of a S809 airfoil for wind turbine application. AIAA Propulsion and Energy Forum and Exposition, 19-22 August 2019.

Rogalla, S., D'Alba, L., Verdoodt, A., Shawkey, M. D. (2019). Hot wings: Thermal impacts of wing coloration on surface temperature during bird flight. Journal of the Royal Society Interface, 16(156).

Samiee, A., Djavareshkian, M. H., Feshalami, B. F., Esmaeilifar, E. (2018). Improvement of airfoils aerodynamic efficiency by thermal camber phenomenon at low Reynolds number. Journal of Aerospace Technology and Management, 10.

Shakeri, R., Al-Garadi, M. A., Badawy, A., Mohamed, A., Khattab, T., Al-Ali, A. K., Harras, K. A., Guizani, M. (2019). Design Challenges of Multi-UAV Systems in Cyber-Physical Applications: A Comprehensive Survey and Future Directions. IEEE Communications Surveys & Tutorials, 21(4), 3340–3385.

Shakhatreh, H., Sawalmeh, A., Al-Fuqaha, A., Dou, Z., Almaita, E., Khalil, I., Othman, N. S., Khreishah, A., Guizani, M. (2018). Unmanned Aerial Vehicles: A Survey on Civil Applications and Key Research Challenges. IEEE Access, vol. 7, pp. 48572-48634.

Sultan, L., Anjum, M., Rehman, M., Murawwat, S., Kosar, H. (2021). Communication among Heterogeneous Unmanned Aerial Vehicles (UAVs): Classification, Trends, and Analysis. IEEE Access, 9, 118815–118836.

Sutherland, W. (1893). LII. The viscosity of gases and molecular force. The London, Edinburgh, and Dublin Philosophical Magazine and Journal of Science, 36(223), 507–531.

Thomas, J. L., Salas, M. D. (1986). Far-field boundary conditions for transonic lifting solutions to the Euler equations. AIAA Journal, 24(7), 1074–1080.

Townsend, A., Jiya, I. N., Martinson, C., Bessarabov, D., & Gouws, R. (2020). A comprehensive review of energy sources for unmanned aerial vehicles, their shortfalls, and opportunities for improvements. In Heliyon (Vol. 6, Issue 11). Elsevier Ltd.

Tucker, V. A. (1993). Gliding Birds: Reduction of Induced Drag by Wing Tip Slots Between the Primary Feathers. In J. exp. Biol (Vol. 180 pp 285-310).

Yu, J. (2018). Design and Optimization of Wing Structure for a Fixed-Wing Unmanned Aerial Vehicle (UAV). Modern Mechanical Engineering, 08(04), 249–263.